The Astrophysical Journal, 888:90 (11pp), 2020 January 10 https://doi.org/10.3847/1538-4357/ab5e84

Rapid Postshock Cooling and Pressure-driven Shell-phase Evolution of the Galactic Halo SNR G70.0–21.5

J. C. Raymond[1], N. Caldwell[1], R. A. Fesen[2], K. E. Weil[1,2], P. Boumis[3], D. di Cicco[4], D. Mittelman[4], and S. Walker[4]
[1] Center for Astrophysics, 60 Garden Street, Cambridge, MA 02176, USA; jraymond@cfa.harvard.edu
[2] 6127 Wilder Lab, Department of Physics & Astronomy, Dartmouth College, Hanover, NH 03755, USA
[3] Institute for Astronomy, Astrophysics, Space Applications and Remote Sensing, National Observatory of Athens, 15236 Penteli, Athens, Greece
[4] MDW Sky Survey, New Mexico Skies Observatory, Mayhill, NM 88339, USA
Received 2019 October 30; revised 2019 November 29; accepted 2019 December 2; published 2020 January 13

Abstract

The large, faint supernova remnant (SNR) G70.0–21.5 is believed to be the result of a Type Ia supernova some 90,000 yr ago at a distance of ∼1 kpc based on the *Gaia* proper motion and parallax of an unusual white dwarf. We have obtained narrow passband optical images and high-resolution spectroscopy to determine shock speeds of 70 to 110 km s^{-1}. The shock itself is unusual in that the sharp Hα filaments arise from a very thin postshock zone where preshock neutral atoms are rapidly excited and ionized. Combining the shock speed with the remnant's estimated age, distance, and diameter, we investigate the SNR evolution in the post-Sedov phase. One-dimensional models that ignore such factors as magnetic fields, cosmic rays, and thermal conduction are marginally consistent with the observations.

Unified Astronomy Thesaurus concepts: Supernova remnants (1667); Shocks (2086)

1. Introduction

G70.0–21.5 is one of the largest and also one of the faintest supernova remnants (SNRs) in the Milky Way. Boumis et al. (2002) were the first to report finding optical filaments located in the constellation Pegasus which they suggested might be part of one or more SNRs. A later study by Fesen et al. (2015), guided by deep Hα images from the Virginia Tech Spectral Line Survey (Dennison et al. 1998; Finkbeiner 2003), found that these Hα filaments comprised a structure some $4\overset{\circ}{.}0 \times 5\overset{\circ}{.}5$ degrees in size, roughly centered at Galactic coordinates $l = 70\overset{\circ}{.}0$, $b = -21\overset{\circ}{.}5$ (R.A.: $21^{h}24^{m}$, Decl.: 19°23′ [J2000]), coincident with faint *ROSAT* X-ray emission along its northern limb. At an estimated distance of ∼1 kpc, it is not only large in its angular size, but also in its 80 pc diameter. Subsequent optical spectra showed that these filaments were indeed shock heated, indicating this filamentary structure is that of a very large SNR situated unusually far off the Galactic plane (Fesen et al. 2015).

Recently, Shen et al. (2018) discovered several high-velocity white dwarfs (WDs) in *Gaia* data, which they identified as candidate remnants of Type I a supernova (SN Ia) explosions in double degenerate systems. One of them, D6–2, has a space velocity of 1200 km s^{-1}, and it is overluminous. Its proper motion can be extrapolated back to near the center of G70.0 −21.5 about 90,000 yr ago, and its 1.0 ± 0.1 kpc distance is similar to that estimated to the SNR. A 1 kpc distance and a Galactic latitude of $-21\overset{\circ}{.}5$ place the SNR some 350 pc out of the plane and well into the Galactic halo. Therefore, the known age and distance of the G70.0−21.5 SNR present a unique opportunity to investigate the late stages of SNR evolution as well as some physical characteristics of the Galactic halo.

A study of the remnant's filaments can also probe the narrow ionization zone just behind a radiative shock in partly neutral gas. Thanks to the low density that the shock is moving through, this zone is marginally resolved. The ratio of [N II] 65,836,548 to Hα intensities indicates a combination of preshock neutral fraction and shock speed, and the line widths of the [N II] and Hα lines serve to indicate the average temperature in the emission region, restricting the range of possible shock parameters.

In addition, many of the remnant's filaments are remarkably straight compared with the faster shocks in younger SNRs such as the Cygnus Loop. G70.0−21.5 has apparently entered the pressure-driven shell phase of SNR evolution, with shocks that are slow enough to be thermally stable. Several studies, including Innes (1992), have shown than shocks slower than about 150 km s^{-1} are thermally stable because the cooling rate rises rapidly with temperature below about 2×10^{5} K, while faster shocks are unstable. Therefore, departures from a simple spherical shape indicate the level of large-scale density inhomogeneity in the Galactic halo.

In Section 2, we present the imaging and spectroscopic observations, Section 3 describes the data analysis, Section 4 presents some shock models and the discussion, and in Section 5 we summarize our results.

2. Observations

2.1. Imaging

Wide-field Hα images of the G70.0−21.5 region were obtained as part of the MDW Hydrogen-Alpha Survey[5] in 2017 November. This survey uses two 0.13 m telescopes at the New Mexico Skies Observatory, each equipped with an FLI ProLine 16,803 CCD and 30 Å FWHM filter centered on Hα. Each telescope−camera system has a field of view of approximately $3\overset{\circ}{.}5 \times 3\overset{\circ}{.}5$ with a pixel size of $3\overset{''}{.}17$. More details are given in di Cicco (2019). A total of nine overlapping regions were combined to form a $9^{\circ} \times 7^{\circ}$ image of the remnant (see Figure 1). Each of the nine images was made from 12×1200 s exposures.

Higher resolution Hα+[N II] (FWHM = 100 Å) and [O III] (λ_c = 5011 Å, FWHM = 49 Å) images of Regions 6 and 7 from Fesen et al. (2015), marked in Figure 1, were taken in

[5] https://www.mdwskysurvey.org

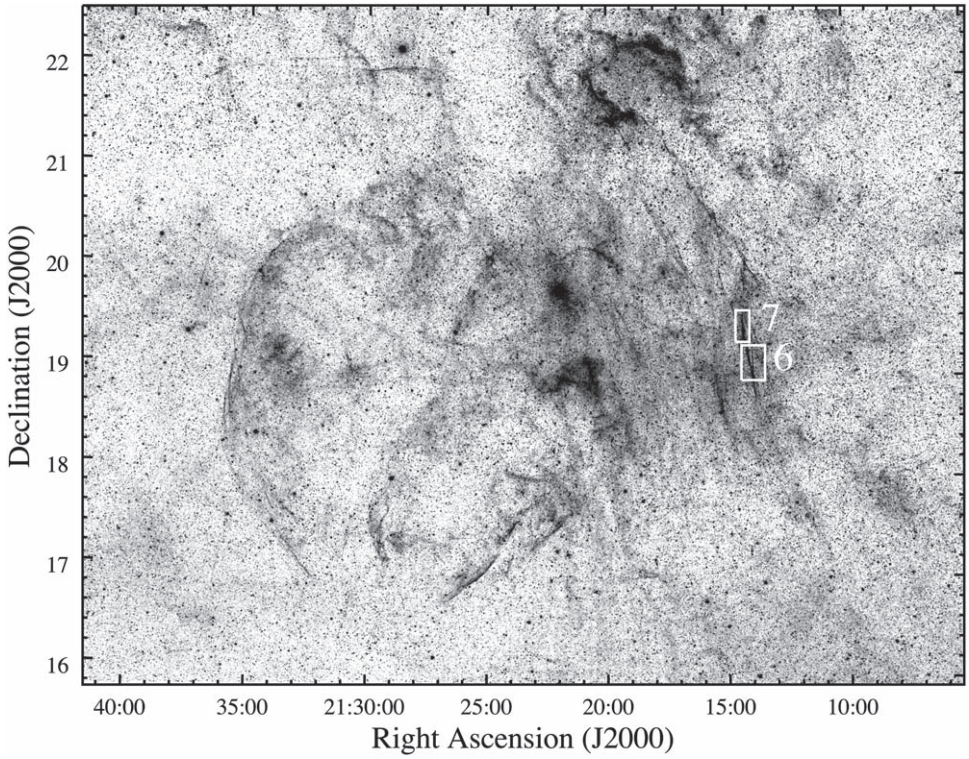

Figure 1. Deep Hα image of G70.0−21.5 from the MDW Hydrogen-Alpha Survey. Regions 6 and 7 from Fesen et al. (2015) are indicated as white boxes.

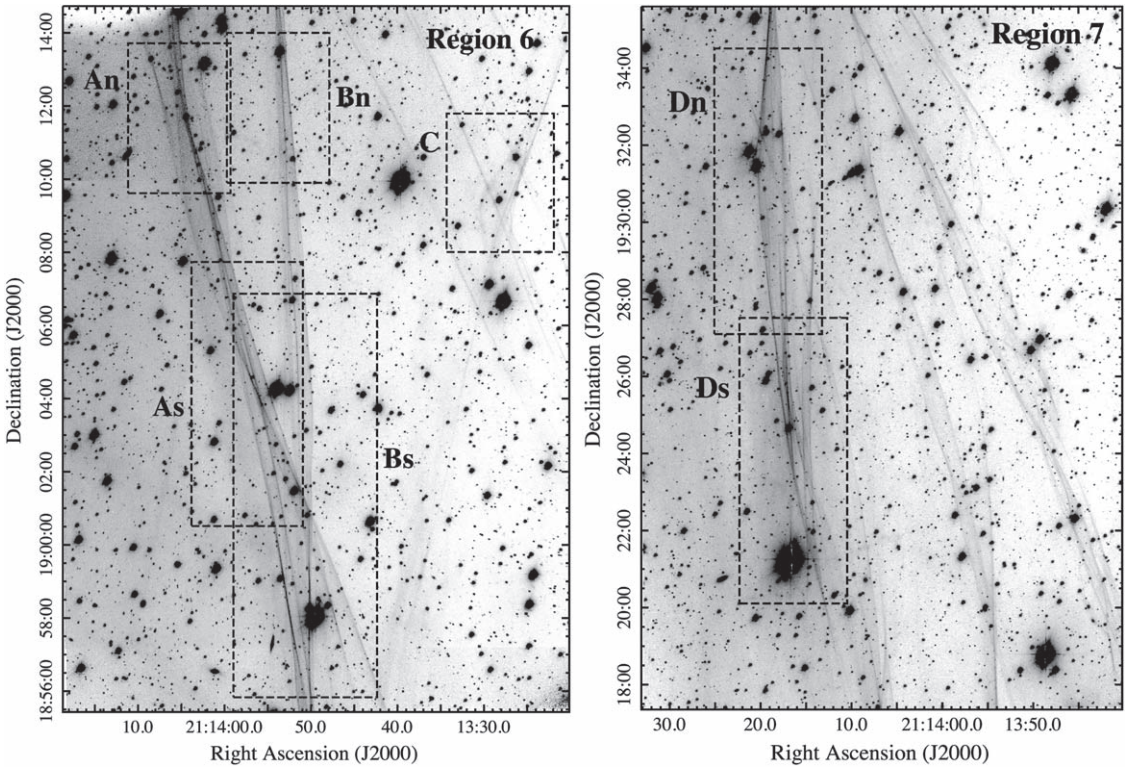

Figure 2. Hα images of Regions 6 and 7. The dashed boxes mark the regions shown in Figures 3–5 which show the positions of the individual Hectochelle fibers for each of the filaments.

2019 September and October using the 2.4 m Hiltner Telescope at MDM Observatory. For each region, two 1000 or 1800 s exposures in each filter were taken using the Ohio State Multi-Object Spectrograph (OSMOS; Martini et al. 2011) and ITL 4064 × 4064 CCD binned 2 × 2. This telescope−instrument system provided an 18.′5 × 18.′5 field of view with a pixel scale of 0.″546. Seeing was between 1″ and 1.″5. Data reduction consisted of CCD amplifier cross-talk correction, bias subtraction, and flat-field correction. The two images in each region were then coadded to remove cosmic rays. The Hα

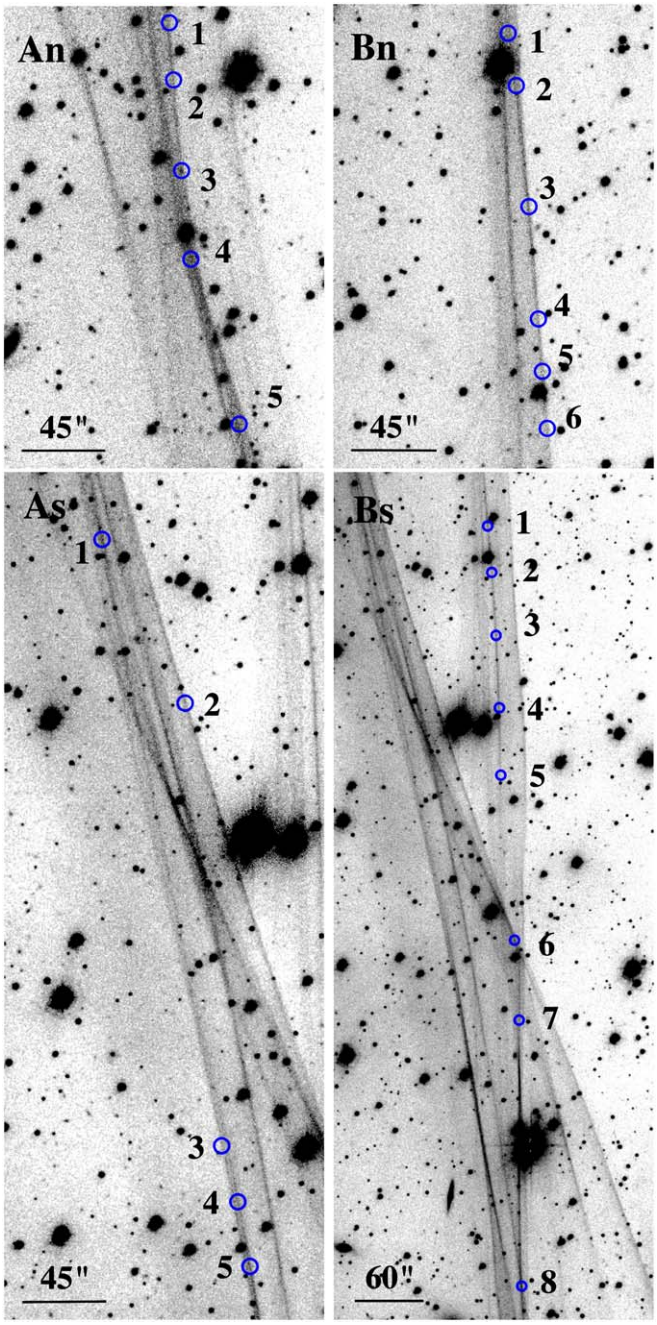

Figure 3. Hα images of Region 6 showing the positions of the Hectochelle fibers for filaments A and B. The blue circles representing the locations of the individual fibers have been enlarged from a diameter of 1.″5 to a diameter of 8″ for clarity. North is up, east is to the left.

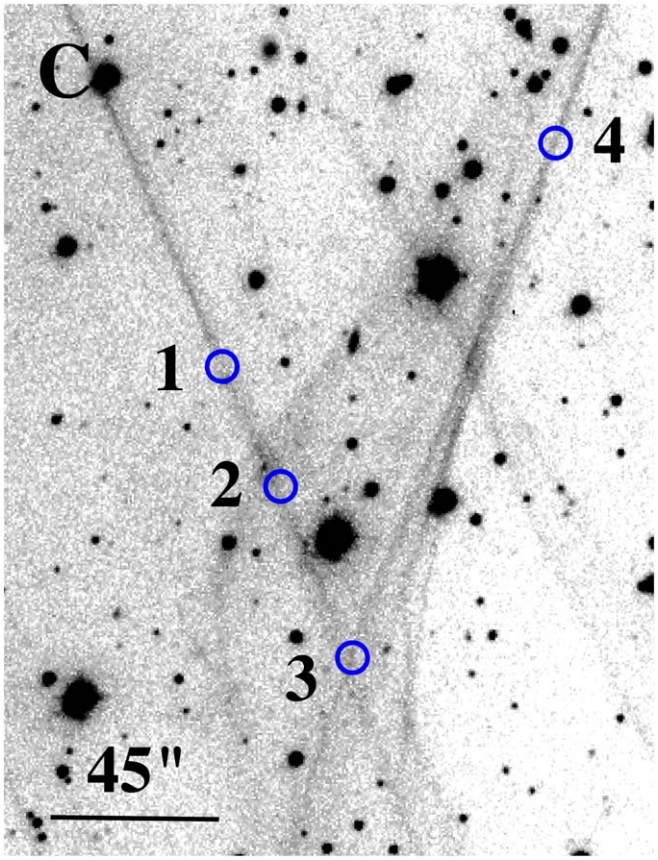

Figure 4. Hα image of Region 6 showing the positions of the Hectochelle fibers for filament C. The blue circles representing the locations of the individual fibers have been enlarged from a diameter of 1.″5 to a diameter of 8″ for clarity. North is to the top, east to the left.

images are shown in Figure 2. Figures 3–5 show expanded versions of the regions where spectra were obtained.

Figure 6 shows a color overlay of the [O III] image on an Hα +[N II] image for Region 7. The Hα emission generally appears as sharp, relatively straight filaments, while [O III] is more diffuse. This contrasts with the radiative shocks in, for instance, the Cygnus Loop, where sharp, well-defined [O III] filaments are followed by patchy, diffuse Hα emission. Extensive diffuse Hα emission is also seen in G70.0–21.5 farther behind the shock. [O III] and Hα are generally correlated along the central north–south ridge, but some regions only appear in Hα (filaments west of center running SW–NE) and some only in [O III] (diffuse band extending from just east of center toward the NW).

Selected filamentary structures from Regions 6 and 7 have been imaged in higher angular resolution with the 2.3 m ($f/8$) Aristarchos telescope at Helmos Observatory in Peloponese, Greece, in 2019 on August 29 and 30. The detector was a 2048 × 2048, 13.5 μm pixel CCD, with a field of view of 5.′5 × 5.′5 (binned × 2, 0.″26 pixel^{-1}). Deep images were taken for 2400 s in Hα + [N II] ($\lambda_c = 6578$ Å, $\Delta\lambda = 40$ Å) and [S II] ($\lambda_c = 6727$ Å, $\Delta\lambda = 40$ Å). The image reduction was carried out using standard IRAF routine packages for the bias subtraction and flat-field correction. During the observations, the "seeing" varied between 0.″9 and 1.″2. Figure 7 compares the (very faint) [S II] emission with that in Hα +[N II]. The [S II] emission shows both diffuse and filamentary components, but the filamentary part is relatively weak compared to that seen in Hα + [N II].

2.2. Spectroscopy

We observed G70.0–21.5 with the Hectochelle instrument on the 6.5 m MMT telescope. Hectochelle (Szentgyorgyi et al. 2011) is a multifiber instrument that obtains single-order spectra through up to 240 optical fibers at a time, covering a wavelength range defined by a blocking filter, in this case covering the 6465 Å–6650 Å range. The fibers can be placed as close together as 25″, and their diameter is 1.″5.

We selected positions along the bright Hα filaments seen in Figure 2 in Regions 6 and 7 of Fesen et al. (2015). The

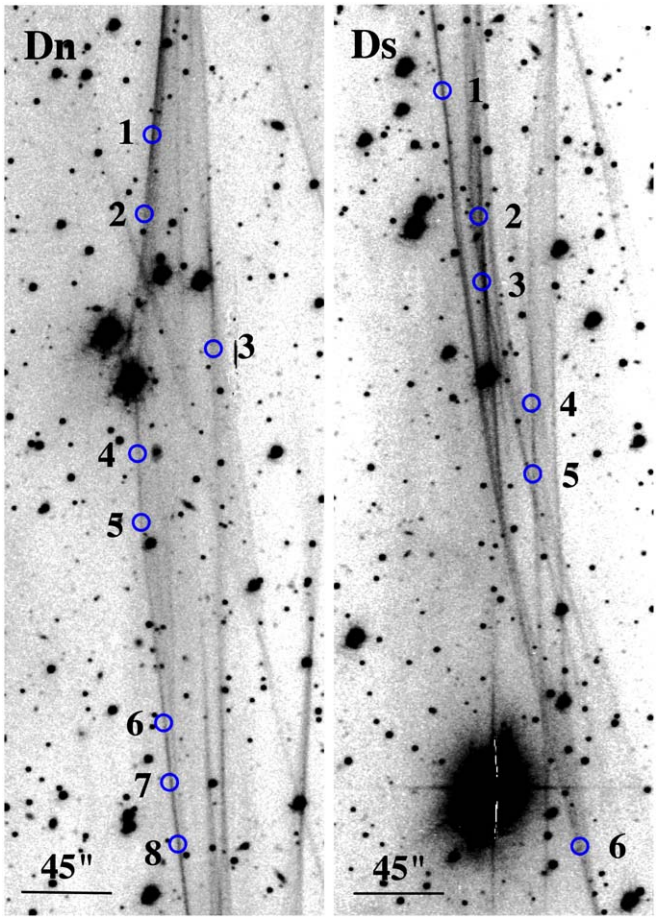

Figure 5. Hα images of Region 7 showing the positions of the Hectochelle fibers for filament D. The blue circles representing the locations of the individual fibers have been enlarged from a diameter of 1.″5 to a diameter of 8″ for clarity. North is to the top, east to the left.

filaments in Region 6 of Fesen et al. (2015) can also be seen in Region F5 of Boumis et al. (2002). Individual fiber positions are shown in Figures 3–5. Hectochelle software optimizes the number of targets from the list of candidate positions and adds additional sky background fibers given the constraint that fibers cannot cross each other. The observations were made on the night of UT 2018 November 30 under partial moon conditions, and two exposures of 45 minutes each were obtained. The seeing was about 1.″1. The data were reduced with the Hectochelle pipeline, including subtraction of dark current, but the night sky was not subtracted from the target spectra. Wavelength calibration is performed as part of the pipeline processing based on thorium–argon comparison spectra taken before and after target exposures. The instrumental resolution based on the widths of the night sky lines was 11 km s^{-1} (FWHM).

The intensity calibration of the Hectochelle counts was achieved by a comparison with the MDM images and spectra presented in Fesen et al. (2015). For that purpose, we used the spectra of Filaments 1 and 2 in Region 3 as shown in Figure 7 of Fesen et al. (2015) to flux calibrate the images. Based on that comparison, we believe that the absolute flux calibration of our spectra is good to about 30%, including a fiber-to-fiber relative throughput variation of about 10%. The relative fluxes of [N II] and Hα depend only on the transmission of the 200 Å wide filter (Szentgyorgyi et al. 2011), and they should be good to better than 10%.

Some of the outlying filaments we observed are quite faint, and we only consider the spectra of the brighter filaments here. We also include only the sky spectra from regions close to the observed filaments, rejecting those at large distances and away from the regions covered by our images. In all, we obtained spectra from 50 positions on the Hα filaments, of which 42 are included in the average spectra discussed below, and we averaged 20 sky positions for the background.

3. Analysis

The only lines detected were Hα and [N II] λ6583. To reach the signal-to-noise needed for accurate [N II] line widths, we have combined the spectra in groups of five to eight fibers in the northern and southern parts of filaments A, B, and D. The region we call C is actually two fainter filaments that cross just outside the main filaments as seen in projection.

It is important to correctly account for the geocoronal contribution to Hα. We define an average sky background from the average of 20 fibers well away from the visible filaments and scale it to minimize the residuals near the night sky lines at 6544, 6554, 6569, and 6577 Å. The ratio of the night sky lines to the background continuum varies somewhat across the field, so we fit the sky spectrum plus a flat background plus a Gaussian to the Hα and [N II] λ6584 lines for each region. While the night sky spectrum is dominated by narrow geocoronal features, some faint Galactic background Hα and [N II] 6584 Å can be seen in the average sky spectrum.

The spectra of the seven regions, along with Gaussian fits are shown in Figure 8. To make the SNR lines easier to see, we show fits to the spectra after subtraction of the night sky lines, along with the night sky spectrum in the lower right. We note that there is no evidence for broad components in the Hα lines that were apparent in the spectra of the Cygnus Loop obtained with Hectochelle (Medina et al. 2014) or FAST (Ghavamian et al. 2001). Medina et al. (2014) studied the ≈350 km s^{-1} nonradiative shocks that produce X-rays in the northern Cygnus Loop. The lack of broad Hα components in G70.0–21.5, along with the presence of [N II] emission, indicates that these are slower, radiative shocks.

The fit parameters are shown in Table 1. The intensities in the table are based on the approximate calibration, and the calibration uncertainty is not included in the error estimate, because we are mainly interested in the [N II]/Hα ratio. Thus, while the [N II]/Hα intensity ratios in the table are reliable, the absolute intensity values are uncertain by perhaps 30%. The [N II] to Hα intensity ratio varies from 0.10 to 0.26. The [N II] line centroids seem be displaced to the red by 6–10 km s^{-1}, or 1σ–2σ. The Hα line widths range from 41 to 61 km s^{-1} (FWHM), while the [N II] lines are 10–25 km s^{-1} narrower, though the uncertainties for some of the [N II] lines are rather large.

4. Interpretation

4.1. Shock Parameters

The first obvious feature of the spectra is that the intensity ratio of [N II] λ6584 to Hα ranges from 0.10 to 0.26 in the observed spectra. That precludes fast nonradiative shocks like those in SN 1006, in which the optical emission arises from a very narrow ionization zone behind a fast collisionless shock.

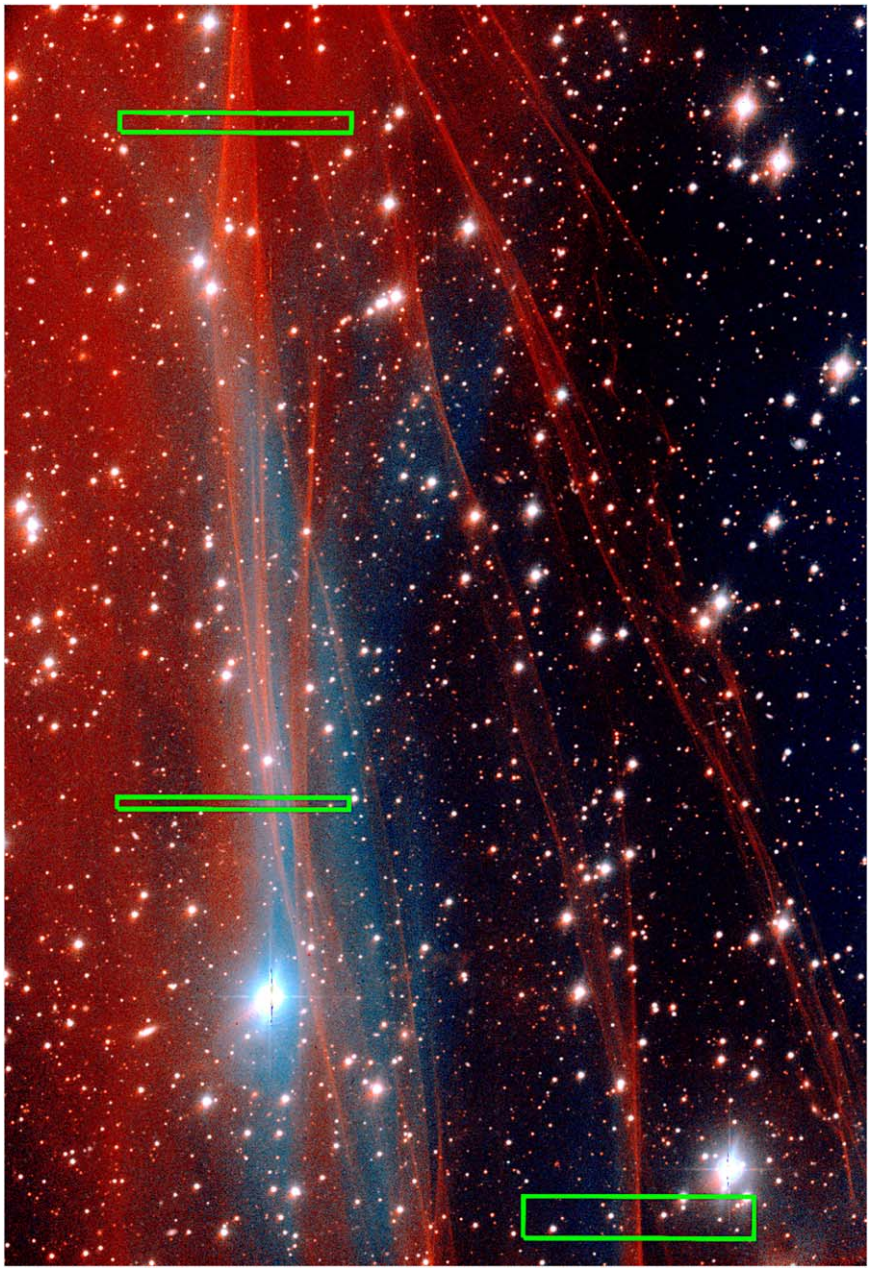

Figure 6. Region 7 in [O III] (blue) and Hα+[N II] (red). The green boxes show the three strips where intensities were extracted to compare the emission in the two lines. In this region, the shock is moving toward the west, and significant diffuse Hα emission is observed in the interior of the shock. The image size is $12\farcm2 \times 18\farcm2$. North is to the top, east to the left.

In those shocks, [N II] and other optical forbidden lines are undetectable (Ghavamian et al. 2001; Medina et al. 2014; Raymond et al. 2017). Those shocks also show two-component Hα line profiles, with a narrow component at the velocity width of the preshock gas and a broad component whose width corresponds to the postshock proton temperature (Chevalier & Raymond 1978).

If we assume that the Hα and [N II] lines are formed at the same temperatures, we can separate the thermal and nonthermal parts of the velocity using

$$W_{\rm OBS}^2 = W_{\rm THERMAL}^2 + W_{\rm BULK}^2 \quad (1)$$

(the observed, thermal, and bulk velocity line widths) and the relation that the thermal speed of nitrogen is $1/\sqrt{14}$ that of hydrogen. For most positions, the uncertainty on the [N II] line width precludes an interesting constraint on the temperature, but for positions Dn and Ds, the hydrogen thermal line widths are around 30–42 km s^{-1}, corresponding to an average temperature of about 29,000 K and bulk line width of around 43 km s^{-1}. A very conservative upper limit to the temperature corresponding to the Hα line width is about 50,000 K. It is not guaranteed that the hydrogen and nitrogen behind a collisionless shock will have the same temperatures, and line widths of fast shocks in SN 1006 yield mass-proportional temperatures, corresponding to equal velocity widths, for H, He, C, N, and O (Korreck et al. 2004; Raymond et al. 2017). However, a slower shock in the Cygnus Loop with a speed of about 350 km s^{-1} shows line widths consistent with equal temperatures for protons, He, and C (Raymond et al. 2015) and electrons

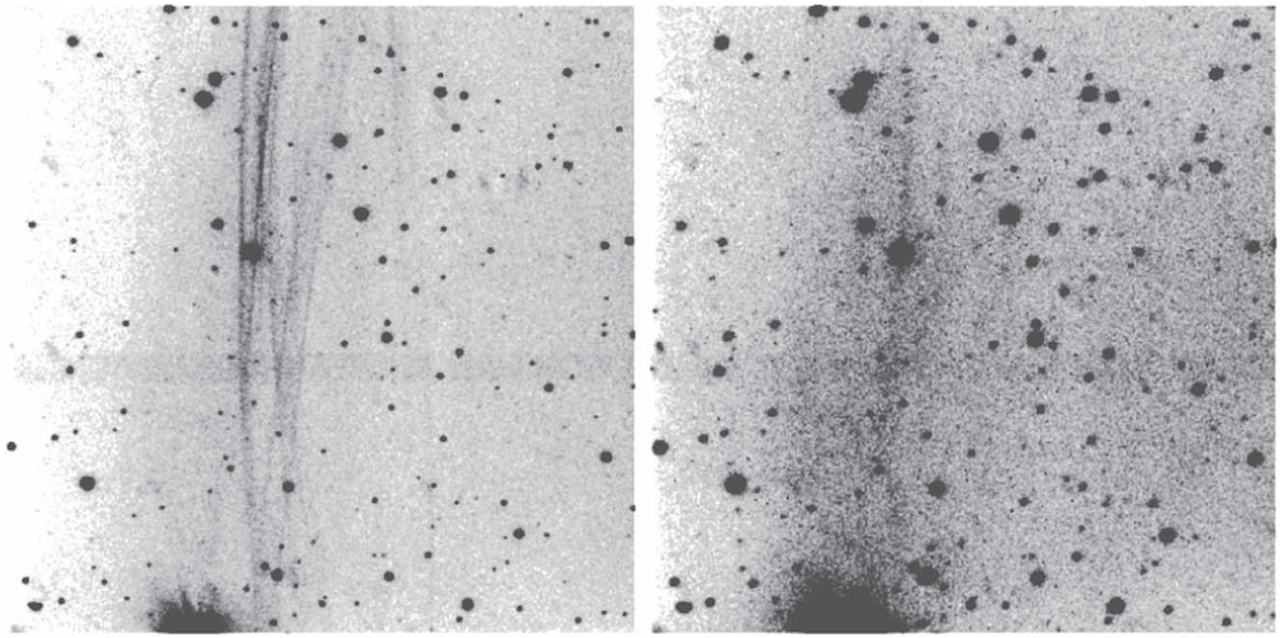

Figure 7. Part of Region 7 in Hα+[N II] (left) and in [S II] (right). The [S II] is extremely faint, but both filamentary and diffuse emission can be seen roughly corresponding to the Hα+[N II] emission. The filamentary component is relatively faint in [S II]. The diffuse horizontal line that appears mostly in the left image is a ghost. The image size is $5\farcm5 \times 5\farcm5$. North is to the top, east to the left.

(Ghavamian et al.2013), so it is probable that the proton and nitrogen kinetic temperatures are the same in the slower shocks in G70.0–21.5.

Table 2 shows the [N II] $\lambda6584/\mathrm{H}\alpha$ intensity ratio and the inferred thermal line width of hydrogen for each of the seven filaments we consider. For filaments Dn and Ds, which have relatively small uncertainties in the [N II] line width, we also show the inferred average kinetic temperature of hydrogen.

Shocks in fully ionized gas generally show [N II]/Hα ratios close to 1, while the ratios measured by Boumis et al. (2002) and Fesen et al. (2015) generally in G70.0–21.5 and those we observe in these western filaments are much smaller. The low ratios can be understood if the preshock gas is partly neutral (Cox & Raymond 1985). In that case the sudden heating by the shock makes it easy to excite the Lyman and Balmer lines of H. The Boltzmann factor in the excitation rate is $e^{(-E_{\rm ex}/kT)}$, where the excitation potential of Hα from the ground state, $E_{\rm ex}$, corresponds to $T = 140{,}000$ K. Therefore, it increases by many orders of magnitude when T jumps from 10^4 to 10^5 K.

The combination of a high excitation rate with the large abundance of H compared to the other elements leads to a cooling rate orders of magnitude larger than in a fully ionized gas at the same temperature. At the same time that the gas is cooling, the neutral hydrogen will be ionizing. Both processes occur in a very narrow region behind the shock because both the cooling and ionization rates are large above 20,000 K. Depending on the shock speed and neutral fraction, the hydrogen can be ionized away, so that the cooling returns to a more normal rate, or so much of the thermal energy can be radiated away and taken up in hydrogen ionization energy that the gas cools to 10,000 K, where the hydrogen ionization and cooling rates become small. In the first case, the spectrum will resemble that of a slower shock in ionized gas, plus strong emission in the Lyman and Balmer lines (Cox & Raymond 1985). In either case, the Balmer lines will be strong compared to other lines.

Many combinations of parameters will produce the observed ratios of [N II] λ6583 to Hα, but we can constrain them. Shock speeds above $110\,\mathrm{km\,s^{-1}}$ photoionize the preshock gas and produce [N II] comparable to Hα, and slower shocks in ionized gas produce unacceptably strong [N II] as well (Hartigan et al. 1987). Shocks slower than $50\,\mathrm{km\,s^{-1}}$ would be unable to produce the observed line widths. Thus, we consider $50 < V < 100\,\mathrm{km\,s^{-1}}$ and preshock neutral fractions above at least 10%. That is consistent with kinetic temperatures of hydrogen near 30,000 K from the line widths, which would be an average over the narrow cooling zone behind the shock. It is also consistent with the spectra shown in Figure 7 of Fesen et al. (2015) except that of filament 4 in Region 5 which shows strong [O III] and requires either a higher shock speed or more highly ionized preshock gas.

We did not observe any positions near Region 5 of Fesen et al. (2015). However, Boumis et al. (2002) show faint, diffuse [O III] emission from the vicinity of our filament A (see their Figure 4), and they detect [O III] in the spectra of 3 of the 11 positions they observed. Such [O III] emission could arise from slow shocks in highly ionized gas or from shocks near $100\,\mathrm{km\,s^{-1}}$. Figure 6 shows the [O III] emission in Region 7, where it is brighter than in Region 6 (Boumis et al. 2002). The [O III] emission is diffuse, rather than concentrated in the narrow postshock ionization zone. It is faint, but consistent with 90–110 $\mathrm{km\,s^{-1}}$ shocks.

To compare the two lines quantitatively, we extracted the average count rates along the three boxes shown in Figure 6, reducing the contribution of stars by taking the median of the emission in the NS direction at each position along the EW direction. The northern and southern slices in Figure 9 show sharp Hα filaments followed by diffuse [O III] peaks about 20″ to the east, as expected from the picture in which the narrow Hα filaments arise in the thin postshock ionization zone. Shoulders on the Hα peaks are seen to the east in the southern cut and to the west in the northern cut. They are probably due to projection as the shock curves away from being tangent to

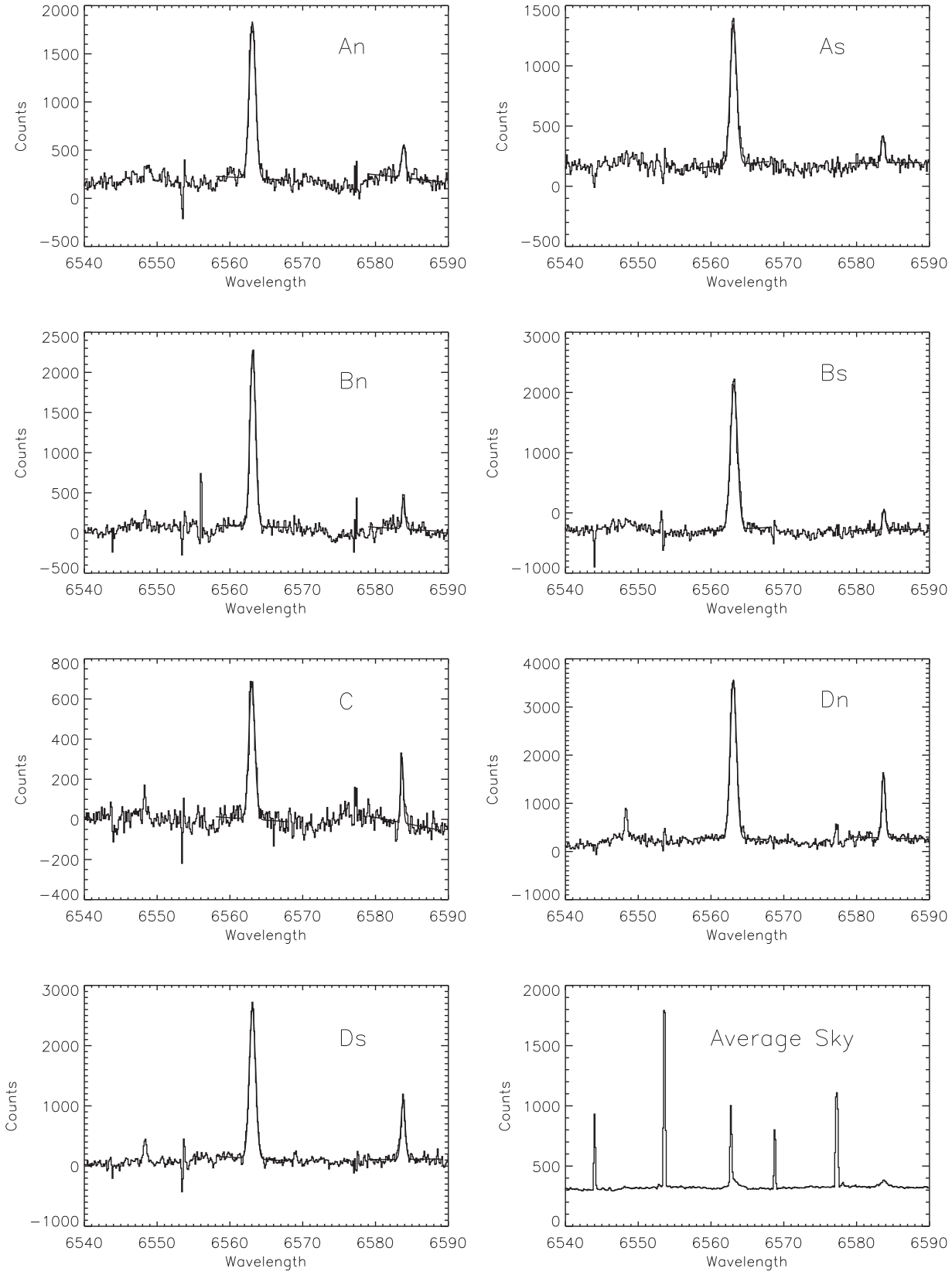

Figure 8. Summed spectra of the fiber groups with Gaussian fits to the Hα and [N II] λ6584 lines. The average spectrum of 20 sky fibers is shown in the lower right.

the line of sight. The cut near the middle of the image is more complex, due to a larger number of filaments where the rippled sheet is tangent to the line of sight, a region seen only in [O III] to the west and a region seen only in Hα to the east. It is not really possible to identify the [O III] with any particular Hα feature or draw any conclusion about the spatial relation between the emission structures of the two lines. The diffuse Hα filling the western part of Figure 6 can be interpreted as the

Table 1
Emission-line Parameters

Fil.	Line	Intensity Rayleighs	Centroid (km s^{-1})	FWHM (km s^{-1})
An	Hα	40.0 ± 2.6	8.8 ± 0.9	57.1 ± 1.0
	[N II]	6.4 ± 1.7	18.3 ± 5.9	46.7 ± 8.0
As	Hα	28.5 ± 1.7	8.6 ± 1.5	56.5 ± 1.0
	[N II]	3.9 ± 1.5	12.3 ± 8.0	43.1 ± 10.7
Bn	Hα	48.7 ± 0.8	11.4 ± 0.9	56.1 ± 1.0
	[N II]	6.7 ± 2.1	18.6 ± 6.3	44.5 ± 10.1
Bs	Hα	63.7 ± 1.8	10.7 ± 0.9	61.4 ± 1.0
	[N II]	6.2 ± 1.7	17.6 ± 5.5	39.0 ± 10.5
C	Hα	18.2 ± 1.2	4.4 ± 1.7	44.9 ± 2.1
	[N II]	4.3 ± 1.2	13.7 ± 5.5	38.9 ± 9.8
Dn	Hα	76.0 ± 2.3	8.5 ± 0.9	55.7 ± 1.0
	[N II]	18.1 ± 1.8	13.8 ± 2.3	40.7 ± 1.1
Ds	Hα	59.5 ± 2.7	9.6 ± 1.9	57.1 ± 1.0
	[N II]	15.4 ± 1.9	15.9 ± 1.7	45.7 ± 1.6

Table 2
Emission-line Parameters

Fil.	[N II]/Hα	FWHM$_{\alpha_T}$ (km s^{-1})	T_H (K)
An	0.16 ± 0.03	33:	
As	0.14 ± 0.06	36:	
Bn	0.14 ± 0.04	34:	
Bs	0.10 ± 0.03	47:	
C	0.24 ± 0.06	22:	
Dn	0.24 ± 0.03	38 ± 4	26,000–39,000
Dn	0.26 ± 0.04	34 ± 4	20,000–30,000

shock-compressed shell of the SNR photoionized by both the EUV emission from the shock and the ambient Galactic and extragalactic EUV background.

We also see that Figure 7 shows [S II] emission, though it is very faint. It is somewhat like the Hα emission in showing filamentary structure, but the filaments are relatively faint compared to the diffuse emission. That is expected if some of the [S II] emission originates in the postshock ionization layer, but it is a smaller fraction. That is natural because the [S II] excitation rate is much less temperature sensitive than the Hα rate, with an excitation potential corresponding to 21,000 K rather than 140,000 K.

There is further indication that some of the Balmer emission arises from collisional excitation in the ionization zone just behind the shock rather than the photoionized recombination zone that dominates the Balmer line emission from radiative shocks above 110 km s^{-1}. Boumis et al. (2002) estimated extinctions A_V in the range 0.6–2.1, corresponding to $E(B-V) = 0.2$ to 0.7. However, the dust maps of Green et al. (2015) and Lallement et al. (2019) show $E(B-V)$ increasing gradually up to 0.1–0.2 at a distance of 1 kpc and remaining flat at larger distances in the direction of G70.0–21.5. The probable explanation is that Boumis et al. (2002) assumed the recombination value of about 3 for the Balmer decrement, while collisional excitation produces ratios of 5 to 3.7 for temperatures of 20,000–40,000 K (CHIANTI; Del Zanna et al. 2015). Thus, for the temperatures estimated in Table 2, $E(B-V)$ could be overestimated by around 0.4–0.5. Variations in the collisional contribution to the Balmer lines would produce variation in the [N II] to Hα ratios seen in Table 2.

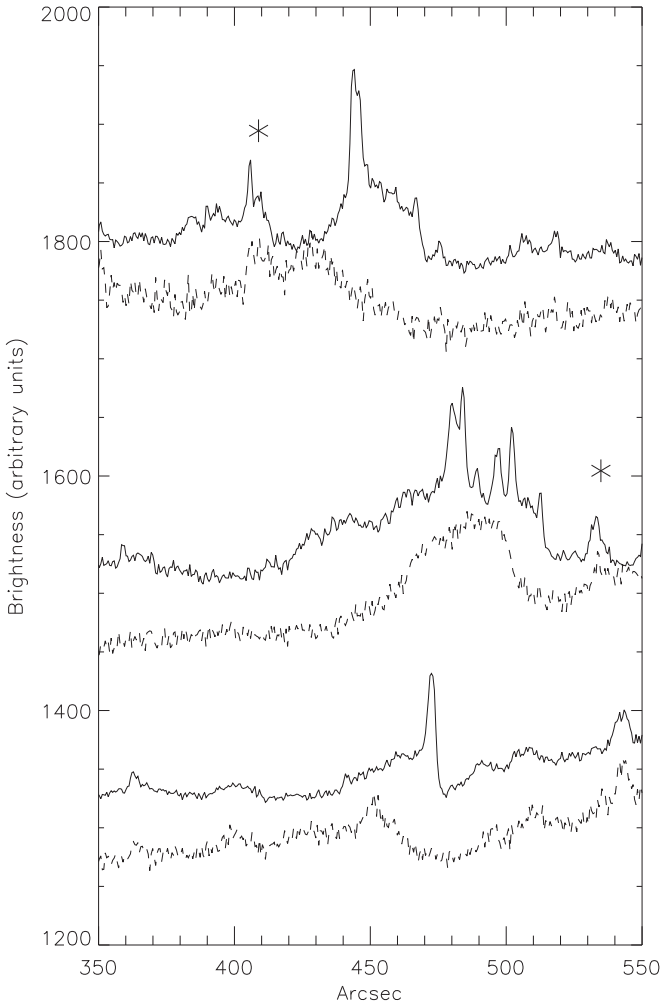

Figure 9. Plots of the Hα (solid) and [O III] (dashed) median intensities along the three strips in Region 7 indicated in Figure 6. The northernmost box corresponds to the uppermost pair of traces. The boxes are 35.″5, 11.″4, and 16.″9 wide. The asterisks indicate stars that were not completely removed by the median filtering.

A complication is that the Hectochelle fibers do not cover the entire postshock cooling region. The 1.″5 in fiber diameter corresponds to about 2.2×10^{16} cm at a distance of 1 kpc. If the ambient density is on the order of 0.2 cm^{-3}, as in the NW Balmer line filaments of the halo SNR SN 1006 (Ghavamian et al. 2002; Bandiera et al. 2019), the cooling distance can be larger than the fiber diameter, though the narrow ionization and cooling zone behind the shock would still fit within a fiber. It is probable that the sharp Hα filaments seen in the MDM images are just the high-emissivity region just behind the shock, and a fainter, cooler, more diffuse region trails behind. That could account for some of the variation in the strengths of the [O I], [N II], and [S II] lines relative to Hα in Figure 7 of Fesen et al. (2015) and Table 3 of Boumis et al. (2002).

To further investigate the line ratios, we ran models with the code described by Raymond (1979) and Cox & Raymond (1985). We assume a preshock density of 0.1 cm^{-3} and a magnetic field of 0.5 μG, and we consider a range of shock speeds from 50 to 90 km s^{-1} and preshock neutral fractions from 0.05 to 0.6. The density choice is based on the height in the Galactic halo, and the magnetic field has little effect on the postshock region where the strong lines are produced. The preshock neutral fraction is determined not only by the overall

Galactic ionizing UV background, but also by the SNR itself. Cox (1972a) showed that an SNR emits a strong burst of ionizing radiation when it enters the shell formation stage, and the recombination time is longer than the SNR evolution timescale. Thus, the preshock gas will be overionized in the case of G70.0–21.5. We truncate the models at distances corresponding to 1.″25. The density could be higher, however, and that makes the cooling region proportionally thinner, so we also consider models truncated at 2.″5 and 5.″0, which correspond to preshock densities of 0.2 and 0.4 cm^{-3}.

In general, a fairly wide range of parameters can match the observed ratio of [N II] to Hα. However, we reject shock speeds below 60 $km\,s^{-1}$ because they predict line widths smaller than we observe. We find that the positions with [N II]/Hα ~0.16 can be matched by 60–80 $km\,s^{-1}$ shocks with preshock neutral fractions of 0.1–0.4 and preshock densities of 0.2–1.0. However, a preshock density as high as 1 is implausible considering the faintness of the filaments and the Galactic halo location, and we find that shock speeds of 60–70 $km\,s^{-1}$ and densities of 0.2–0.4 cm^{-3} are likely. For the filaments showing [N II]/Hα ~0.25, we find that shock speeds of 50–90 $km\,s^{-1}$ are acceptable with neutral fractions of 0.1–0.4 and densities around 0.2 to 0.4 cm^{-3}. The models generally predict [O I] and [S II] line strengths similar to those seen in Table 3 of Boumis et al. (2002) and Figure 7 of Fesen et al. (2015) when integrated over larger lengths corresponding to the spatial sampling of those spectra.

On the other hand, the presence of [O III] at some positions indicates that somewhat faster shocks may be present (see Figure 6). The [O III] emission is diffuse, but it seems to roughly correspond to the Hα emission, and it is brighter in the northern (Region 7) area. The presence of neutral H in the preshock gas, as indicated by the high Hα/[N II] ratios, indicates that oxygen is not doubly ionized ahead of the shock, because of the rapid charge transfer between O^{++} and H I. Therefore, the [O III] indicates shock speeds of about 100 $km\,s^{-1}$ or more. The [O III] emission is detected on only about one-quarter of the spectra of Boumis et al. (2002) and Fesen et al. (2015), and it is faint in the images, so we conclude that the shock speed ranges from roughly 70 to roughly 110 $km\,s^{-1}$. Faster shocks in more neutral gas could produce the faint [O III] emission, but then Hα from the ionization zone would show temperatures above 50,000 K.

4.2. Global Parameters of G70.0–21.5

The association of WD D6–2 with the SNR implies a distance of ~1 kpc and an age of 90,000 yr (Shen et al. 2018). While the proper motion has an uncertainty of less than 1%, the age estimate also depends on the position of the SNR center. That uncertainty appears to be on the order of a tenth of the distance between the WD and the center, so we adopt an uncertainty of 10% on the age and take it to be 80,000 to 100,000 yr. Similarly, the uncertainty on the parallax is 11% (3σ), which contributes to the uncertainty in the distance to the SNR and therefore in its radius. The apparent size is 4° to 5° in radius, so adding in the distance uncertainty in quadrature, we take the radius of the SNR to be 40 ± 6 pc.

Neither the SN energy nor the preshock interstellar density is known. We will assume a reference value of 10^{51} erg and ask whether that can match the observed radius and shock speed. The expected density of the Galactic halo at a height of 360 pc is around 0.071 cm^{-3} (Cox 2005). The filaments we observed are 5 to 20 times fainter than the bright Hα filaments in the Cygnus Loop where preshock densities are believed to be 2–5 cm^{-3} (Miller 1974; Raymond et al. 1988, 2001). Therefore, we expect preshock densities of 0.1–0.4 cm^{-3} in G70–21.5. The gas must have a significant neutral fraction in order to explain the high Hα/[N II] ratios, probably higher than the ~0.1 neutral fraction inferred for the NW region of SN 1006 about 500 pc from the plane (Ghavamian et al. 2002). The fairly complete shell suggests that cool, partly neutral gas fills much of the volume in this region. The overall circular shape suggests fairly uniform density, but the brightness variation suggests increasing density toward the Galactic plane.

4.3. Comparison with SNR Evolution Models

Because the radius, shock speed and age of the SNR are known, it is worthwhile to compare them with models of SNR evolution. The magnetic plus cosmic-ray pressure at 360 pc is around 1.6×10^{-12} dyne cm^{-3} (Cox 2005), which is about 10% of the ram pressure of a 100 $km\,s^{-1}$ shock in a density of 0.071 cm^{-3}. These nonthermal pressures should have a modest, but perhaps not negligible, effect on the evolution at late times. For now we will ignore them.

It is expected that a remnant will follow the Sedov solution until radiative cooling sets in at an age of 61, 40, 30, or 25 thousand years for densities of 0.1, 0.2, 0.3, or 0.4 cm^{-3}, respectively (Cox 1972b). Consequently, G70.0–21.5 has clearly entered the post-Sedov phase, as expected from the relatively slow radiative shocks observed. Cioffi et al. (1988) fit a numerical simulation of SNR evolution in the pressure-driven shell phase to analytic functions, which are shown in Figure 10. A radius of 40 ± 6 pc at an age of 90,000 ± 10,000 yr is compatible with densities between 0.1 cm^{-3} (46 pc, 80,000 yr) and 0.4 cm^{-3} (35 pc, 100,000 yr). However, the predicted shock speeds range from 110 $km\,s^{-1}$ (0.4 cm^{-3}, 35 pc, 100,000 yr) to 190 $km\,s^{-1}$ (0.1 cm^{-3}, 46 pc, 80,000 yr). Within the uncertainties, it is barely possible to match a radius of 35 pc and a shock speed of 110 $km\,s^{-1}$ with a preshock density of 0.4 cm^{-3} and an age of 100,000 yr. However, that density is unexpectedly high for gas 360 pc from the plane, and the faintness of [O III] indicates that 110 $km\,s^{-1}$ is at the upper end of the range of shock speeds. There is a short period when the SNR is undergoing the transition from Sedov to radiative phases when the sudden drop in pressure causes a sharp dip in the shock speed, but in the Cioffi et al. (1988) model that occurs at an age younger than that of G70.0-21.5.

On the theoretical side, the model of Cioffi et al. (1988) ignores the magnetic field contribution to the pressure (Chevalier 1974; Petruk et al. 2018), cosmic-ray pressure (Lee et al. 2015), and thermal conduction (Cox et al. 1999). For typical interstellar medium (ISM) parameters, magnetic and cosmic-ray pressures are small immediately behind the shock where the Hα filaments are formed, but they can dominate as the gas cools and further compression increases those components of nonthermal pressure. The model also ignores cooling by dust, which is typically an order of magnitude stronger than X-ray cooling (Koo et al. 2016) and the effects of an inhomogeneous ISM, which can reduce the shell momentum at very late times by a factor of 2 (Pittard 2019). Moreover, the behavior of even the 1D model is complicated near the time of shell formation, and the analytic fit of Cioffi et al. (1988) is less accurate there. We have also assumed an explosion energy of 1×10^{51} erg. A different energy is possible, but the ratio of

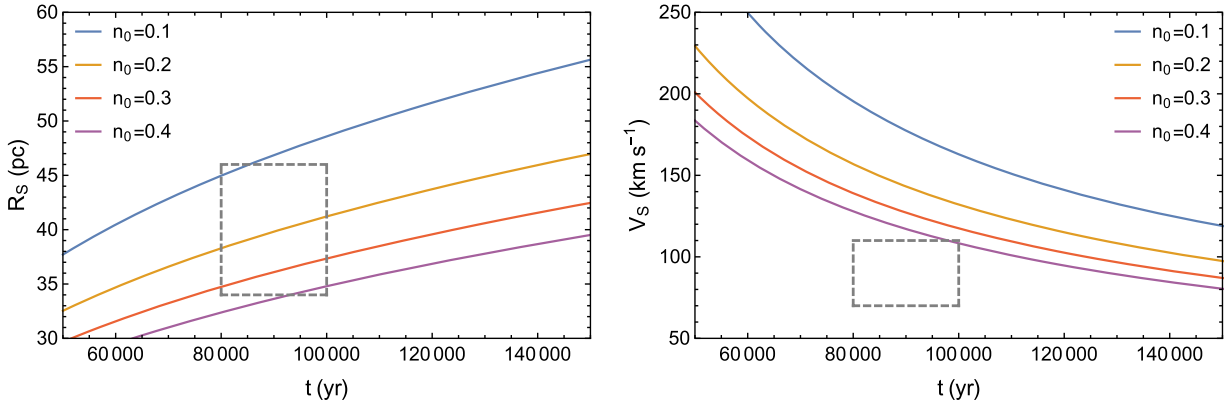

Figure 10. Radius and velocity as functions of time for four ambient densities from Cioffi et al. (1988). An explosion energy of 10^{51} erg was assumed. The boxes represent the limits as derived from the observables. On the left, the minimum and maximum radii give the remnant's distance, and on the right, the minimum and maximum velocity estimated from the structure of the shocks.

V_S/R in the pressure-driven shell phase scales as $n_0^{4/7}E_0^{-3/14}$ (Cioffi et al. 1988), and a drastic difference in E_0 is needed to have much effect on the shock speed. Therefore, it is likely that one or more of the factors ignored in the 1D model has a noticeable effect on the SNR evolution.

5. Summary

G70.0–21.5 is a large, faint SNR in the Galactic halo. Its connection with a high-velocity WD (Shen et al. 2018) establishes its age as 90,000 ± 10,000 yr and its distance as 1.0 ± 0.1 kpc. Knowledge of those two parameters makes it uniquely suited to investigations of SNR evolution in the pressure-driven shell phase.

We have obtained high-resolution profiles of the Hα and [N II] lines from a number of filaments at the western edge of the SNR. Comparison of the high Hα/[N II] intensity ratios with shock models and the presence of [O III] in some positions indicate modest shock speeds of 70–110 km s^{-1} and a significant neutral fraction in the preshock gas. The hydrogen kinetic temperature obtained from the widths of the Hα and [N II] lines is 20,000 to 40,000 K, indicating that the emission arises from the narrow zone of ionization and cooling just behind the shock, where the preshock neutrals are partially or entirely ionized away (Cox & Raymond 1985). That interpretation is corroborated by the small thickness of the Hα filaments, which would be ∼10″ thick for the full cooling zone at the densities of the Galactic halo.

Comparison with the SNR evolution model of Cioffi et al. (1988) shows that the observed age, size, and velocity are marginally consistent with a preshock density of 0.4 cm^{-3}, but that is a much higher density than expected for a height of 360 pc from the Galactic plane. There are several simplifications (ignoring magnetic fields, cosmic-ray pressure, thermal conduction, dust cooling, and density inhomogeneities) in the existing models that might be responsible for the discrepancy, but more extensive observations that would help to pin down the shock speed at different locations around the SNR are required.

We thank the staff of the MMT telescope for carrying out the Hectochelle observations. We thank Eric Galayda and the MDM staff for assistance with our observations. K.E.W. acknowledges support from Dartmouth's Guarini School of Graduate and Advanced Studies, and the *Chandra* X-ray Center under CXC grant GO7-18050X. The "Aristarchos" telescope is operated on Helmos Observatory by the Institute for Astronomy, Astrophysics, Space Applications and Remote Sensing of the National Observatory of Athens. CHIANTI is a collaborative project involving George Mason University, the University of Michigan (USA), University of Cambridge (UK), and NASA Goddard Space Flight Center (USA).

Facilities: MMT (Hectochelle), Hiltner (OSMOS).

ORCID iDs

J. C. Raymond https://orcid.org/0000-0002-7868-1622
N. Caldwell https://orcid.org/0000-0003-2352-3202
R. A. Fesen https://orcid.org/0000-0003-3829-2056
K. E. Weil https://orcid.org/0000-0002-8360-0831

References

Bandiera, R., Morlino, G., Knežević, S., & Raymond, J. C. 2019, MNRAS, 483, 1537
Boumis, P., Mavromatakis, F., Paleologou, E. V., & Becker, W. 2002, A&A, 396, 225
Chevalier, R. A. 1974, ApJ, 188, 501
Chevalier, R. A., & Raymond, J. C. 1978, ApJL, 225, 27
Cioffi, D. F., McKee, C. F., & Bertschinger, E. 1988, ApJ, 334, 252
Cox, D. P. 1972a, ApJ, 178, 143
Cox, D. P. 1972b, ApJ, 178, 159
Cox, D. P. 2005, ARA&A, 43, 337
Cox, D. P., & Raymond, J. C. 1985, ApJ, 298, 651
Cox, D. P., Shelton, R. L., Maciejewski, W., et al. 1999, ApJ, 524, 179
Del Zanna, G., Dere, K. P., Young, P. R., Landi, E., & Mason, H. E. 2015, A&A, 582, 56
Dennison, B., Simonetti, J. H., & Topasna, G. A. 1998, PASA, 15, 147
di Cicco, D. 2019, S&T, 138, 20
Fesen, R. A., Neustadt, J. M. M., Black, C. S., & Koeppel, A. H. D. 2015, ApJ, 812, 37
Finkbeiner, D. P. 2003, ApJS, 146, 407
Ghavamian, P., Raymond, J. C., Smith, R. C., & Hartigan, P. 2001, ApJ, 547, 995
Ghavamian, P., Schwartz, S. J., Mitchell, J., Masters, A., & Laming, J. M. 2013, SSRv, 178, 633
Ghavamian, P., Winkler, P. F., Raymond, J. C., & Long, K. S. 2002, ApJ, 572, 888
Green, G. M., Schlafly, E., Finkbeiner, D. P., et al. 2015, ApJ, 810, 25
Hartigan, P., Raymond, J., & Hartmann, L. 1987, ApJ, 316, 323
Innes, D. E. 1992, A&A, 256, 660
Koo, B.-C., Lee, J.-J., Jeong, I.-G., Seok, J. Y., & Kim, H.-J. 2016, ApJ, 821, 20
Korreck, K. E., Raymond, J. C., Zurbuchen, T. H., & Ghavamian, P. 2004, ApJ, 615, 280
Lallement, R., Babusiaux, C., Vergely, J. L., et al. 2019, A&A, 625, 135

Lee, S.-H., Patnaude, D. J., Raymond, J. C., et al. 2015, ApJ, 806, 71
Martini, P., Stoll, R., Derwent, M. A., et al. 2011, PASP, 123, 187
Medina, A. A., Raymond, J. C., & Edgar, R. E. 2014, ApJ, 791, 30
Miller, J. S. 1974, ApJ, 189, 239
Petruk, O., Kuzyo, T., Orlando, S., et al. 2018, MNRAS, 479, 4253
Pittard, J. M. 2019, MNRAS, 488, 3376
Raymond, J. C. 1979, ApJS, 39, 1
Raymond, J. C., Edgar, R. J., Ghavamian, P., & Blair, W. P. 2015, ApJ, 805, 152
Raymond, J. C., Hester, J. J., Cox, D., et al. 1988, ApJ, 324, 869
Raymond, J. C., Li, J., Blair, W. P., & Cornett, W. H. 2001, ApJ, 560, 763
Raymond, J. C., Winkler, P. F., Blair, W. P., & Laming, J. M. 2017, ApJ, 851, 12
Shen, K. J., Boubert, D., Gänsicke, B. T., et al. 2018, ApJ, 865, 15
Szentgyorgyi, A., Furesz, G., Cheimets, P., et al. 2011, PASP, 123, 1188